Journal of Geophysical Research: Solid Earth

RESEARCH ARTICLE
10.1029/2017JB015408

Key Points:
- Earthquakes within 1 km from the main faults in the area have distinctly different properties than events between and off the faults
- Aftershock sequences of five M > 4.5 earthquakes have different spatial properties and little overlap with each other
- Analyzing the events as occurring along a single surface or narrow zone may lead to erroneous inferences

Supporting Information:
- Supporting Information S1
- Data Set S1
- Data Set S2
- Data Set S3
- Data Set S4

Correspondence to:
Y. Cheng,
chengyif@usc.edu

Citation:
Cheng, Y., Ross, Z. E., & Ben-Zion, Y. (2018). Diverse volumetric faulting patterns in the San Jacinto fault zone. *Journal of Geophysical Research: Solid Earth*, *123*, 5068–5081. https://doi.org/10.1029/2017JB015408

Received 26 DEC 2017
Accepted 21 MAY 2018
Accepted article online 27 MAY 2018
Published online 16 JUN 2018

Diverse Volumetric Faulting Patterns in the San Jacinto Fault Zone

Yifang Cheng[1], Zachary E. Ross[2], and Yehuda Ben-Zion[1]

[1]Department of Earth Sciences, University of Southern California, Los Angeles, CA, USA, [2]Seismological Laboratory, California Institute of Technology, Pasadena, CA, USA

Abstract We examine locations, magnitudes, and faulting types of post-2000 earthquakes in the trifurcation area of San Jacinto fault zone to clarify basic aspects of failure processes in the area. Most M ≥ 3.5 events have strike-slip mechanisms, occur within 1 km of the main faults (Clark, Buck Ridge, and Coyote Creek), and have hypocenter depths of 10–13 km. In contrast, many smaller events have normal source mechanisms and hypocenters in intrafault areas deeper than 13 km. Additional small events with hypocenter depth <13 km occur in off-fault regions and have complex geometries including lineations normal to the main faults. Five moderate earthquakes with M 4.7–5.4 have high aftershock rates (~150 M ≥ 1.5 events within 1 day from the mainshock). To obtain more details on aftershock sequences of these earthquakes, we detect and locate additional events with the matched filter method. There are almost no aftershocks within 1 km from the mainshocks, consistent with large mainshock stress drops and low residual stress. The five aftershock sequences have almost no spatial overlap. While the mainshocks are on the main faults, most aftershocks are located in intrafault and off-fault regions. Their locations and spatial distribution reflect the mainshock rupture directions, and many also follow structures normal to the main faults. The significant diversity of observed features highlights the essential volumetric character of failure patterns in the area. The increasing rate of moderate events, productive aftershock sequences, and large inferred stress drops may reflect processes near the end of a large earthquake cycle.

1. Introduction

The standard model for earthquake and fault mechanics assumes that moderate and large earthquakes can be described to first order in terms of slip along a single (potentially heterogeneous) surface in a continuum solid (e.g., Ben-Zion & Sammis, 2003; Tse & Rice, 1986). This model is used widely in theoretical research and analyses of seismic and geodetic data (e.g., Hillers et al., 2006; Thomas et al., 2017), although some studies adopt granular mechanics, damage rheology, and other frameworks that emphasize the simultaneous failure of, and interactions between, networks of slipping regions (e.g., Ben-Zion, 2008, and references therein). Inspections of rupture properties of well-recorded large earthquake such as (among many) the 1992 Mw7.3 Landers (e.g., Hauksson et al., 1993), 2010 M_W 7.2 El Mayor-Cucapah (e.g., Wei et al., 2011), 2012 M_W 8.6 Indian Ocean (e.g., Yue et al., 2012), 2016 Mw 7.0 Kumamoto (e.g., Asano & Iwata, 2016; Shirahama et al., 2016), and 2016 Mw 7.8 Kaikoura (e.g., Clark et al., 2017; W. Xu et al., 2018) earthquakes, and seismicity patterns in well-instrumented areas (e.g., California, Taiwan, Japan), indicate that complex volumetric failure patterns of fault networks are common rather than the exception. This suggests that efforts to collapse the dynamics of moderate and large earthquakes to single surfaces may miss important aspects of the physics governing earthquake behavior. In the present paper, we analyze detailed seismicity patterns associated with several moderate earthquakes in the San Jacinto fault zone (SJFZ) in southern California in an effort to clarify basic characteristics of earthquake dynamics. The SJFZ provides a good natural laboratory for detailed studies of earthquake dynamics because it is highly active and well instrumented. The observed results are likely to be relevant to earthquake processes in other areas. We note that various processes such as rock fracturing and deviations from planarity can produce isotropic source terms (e.g., Ben-Zion & Ampuero, 2009; Julian et al., 1998; Ross et al., 2015) that can be important for the local physics. However, here we focus on larger-scale phenomena involving the occurrence of earthquakes in geometrically complex crustal volumes that cannot be approximated by surfaces or narrow tabular zones.

The SJFZ is the most seismically active fault zone in southern California (Hauksson et al., 2012) and accommodates a large portion of the plate motion in the region (e.g., Fay & Humphreys, 2005; Lindsey & Fialko, 2013). Since 1890, the SJFZ produced 11 M_W > 6 earthquakes (Wdowinski, 2009), and paleoseismic records indicate

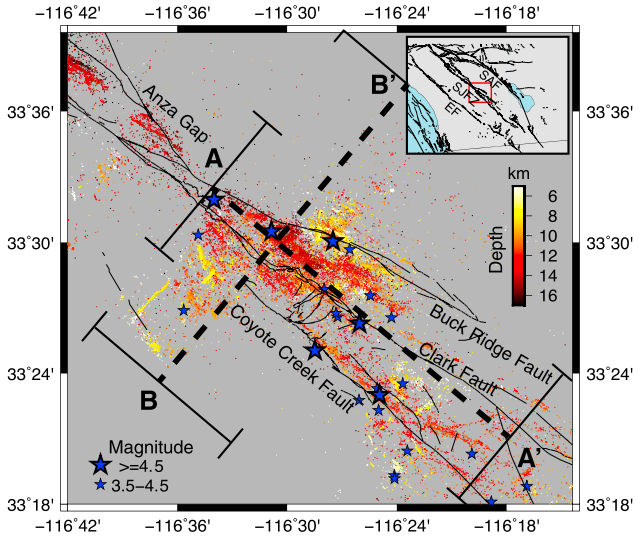

Figure 1. Map view of 2000–2016 seismicity (dots and stars) and main faults (thin solid lines) in the trifurcation area of the San Jacinto fault zone. The dashed lines indicate cross sections used in Figure 2. The inset shows the location of the study area (red box) in southern California along with the entire San Jacinto fault zone (SJFZ), San Andreas Fault (SAF), and Elsinore Fault (EF).

that it is capable of larger events (e.g., Onderdonk et al., 2013; Petersen & Wesnousky, 1994; Rockwell et al., 2015) that pose significant seismic hazard to large urban areas in southern California. The Anza seismicity gap in the central SJFZ is notable due to a lack of microseismicity and moderate to large earthquakes in the previous century (Sanders & Kanamori, 1984). In the trifurcation area located to the southeast of the Anza gap, the SJFZ branches into the Coyote Creek, Clark, and Buck Ridge faults (Figure 1). In contrast to the seismic quiescence in the Anza gap, since 2000 more than 10% of all detected earthquakes in Southern California have occurred in the trifurcation area. Since 1 January 2000, four earthquakes with $M_L \geq 5$ occurred in the trifurcation area (Figure S1 in the supporting information). For comparison, only three $M_L \geq 5$ events occurred from 1932 to 1999 along the entire 100-km-long Clark fault in the SJFZ (in 1937, 1963, and 1980, respectively). The recent frequent moderate earthquakes and high rate of ongoing seismicity in the trifurcation area suggest increasing potential for the occurrence of large earthquake on the SJFZ (e.g., Zöller & Ben-Zion, 2014). The analysis done in this study helps to probe processes associated with the possible approach of a large earthquake in the region.

The depth extent of seismogenic faults is essential for estimating the possible rupture area, magnitude and seismic hazard associated with large events. Wdowinski (2009) noted a significant discrepancy between the geodetically inferred locking depth in the trifurcation area and maximum depth of seismicity, and suggested that the deeper events reflect a deep creeping zone below the SJFZ. Meng and Peng (2016) analyzed seismicity associated with 10 $M > 4$ earthquakes after 2000 and found that mainshocks with hypocenters depth below 11 km have significantly larger aftershock zones than shallower events with comparable magnitudes. However, these studies assumed implicitly that all examined events (moderate mainshocks and microseismicity) essentially occur on the main fault plane. Ross, Hauksson, and Ben-Zion (2017) analyzed aftershocks of the 2016 Mw 5.2 Borrego Springs earthquake and observed complex volumetric patterns with distinctly different spatial and frequency-size event properties within 1 km of the main faults and those in the surrounding region. While the moderate earthquakes are located on the main faults, much of the lower magnitude events including many deep events are in a broad damage zone around the main faults (Figures 1 and 2). Projecting all events to a single surface as done in many analyses may lead to erroneous inferences.

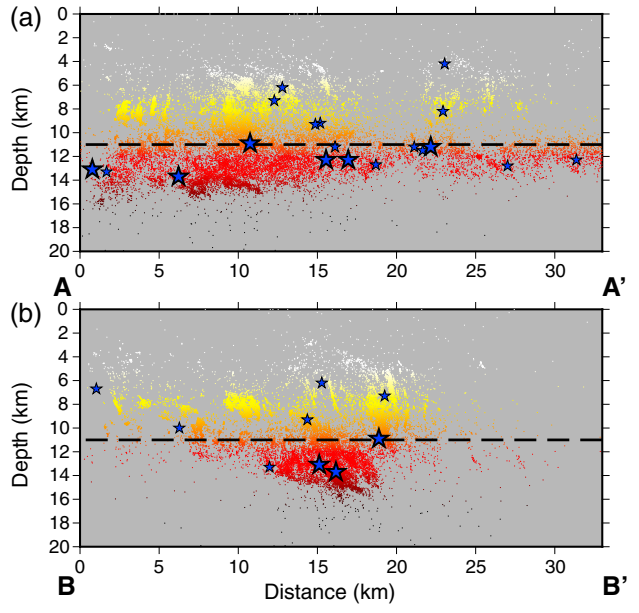

Figure 2. Depth profile of seismicity along (a) A-A′ and (b) B-B′ in Figure 1. Dashed lines indicate the estimated geodetic locking depth from Fialko (2006).

To analyze characteristics associated with additional moderate events in the trifurcation area and unravel key aspects of the evolving earthquake failure processes in relation to the main faults, we investigate in detail lateral and depth variations of seismicity and focal mechanisms in the region. We examine both the overall earthquake population based on the regional seismic catalog from 2000 to 2016 (Figures 1 and 2) and detailed features associated with five $M > 4.5$ events (Table 1) and their aftershock sequences. In the next section, we describe the data used in the study. In section 3 we present results on spatiotemporal-magnitude-mechanism patterns in different crustal volumes in the trifurcation area of the SJFZ. The results highlight the essential volumetric character and diversity of failure processes in the area. The aftershock sequences of the $M > 4.5$ events have very little overlap and occur collectively in a broad damage zone. The depth of seismicity is near the geodetic locking depth close to the main faults and is significantly deeper in the outer regions. These and other aspects of the results are discussed in the final section 4.

Table 1
Details of the M ≥ 4.5 Earthquakes Shown in Figure 1

Date	Time	Longitude	Latitude	Depth (km)	*M*	Template events no.	No. of differential time used in relocation	Event no. after detection and relocation
10/31/2001	07:56:16	−116.514	33.508	13.7	5.0	484	2,294,006	6211
06/12/2005	15:41:46	−116.567	33.532	13.1	5.2	897	690,004	6031
07/07/2010	23:53:33	−116.475	33.417	12.3	5.4	1506	3,352,111	10328
03/11/2013	16:56:06	−116.458	33.501	10.9	4.7	1331	9,181,498	9288
06/10/2016	08:04:39	−116.443	33.431	12.3	5.2	1619	28,000,000	12487

2. Data

The study is based on several different data sets. We use 25 M ≥3.5 earthquakes from Southern California Seismic Network (SCSN) standard catalog (nonrelocated). An additional data set with 44,153 M < 3.5 events (2000–2016; Figures 1–3) is based on the relocated southern California catalog (Hauksson et al., 2012) and its most recent update (http://scedc.caltech.edu). The locations of larger magnitude (M ≥ 3.5) events are taken from the standard (rather than relocated) catalog, since the largest events do not correlate well with small ones. We also use 20,802 focal mechanism solutions (2000–2016) from the catalog of Yang et al. (2012) and its most recent update.

The continuous waveform data at 28 stations are used to detect additional earthquakes during five highly active seismic sequences (Figure S2) listed in Table 1. Of these stations, there are 15 broadband sensors from the AZ network (Fletcher et al., 1987), 6 borehole seismometers from the Plate Boundary Observatory network (since 2006), and 7 broadband stations from the CI network (Hutton et al., 2010). Aftershock sequences in 2001 and 2005 are recorded only by the AZ network, while sequences in 2010, 2013, and 2016 are recorded by the AZ, CI, and PB networks (Figure S2). For each sequence, we use all available continuous waveform data from the Southern California Earthquake Data Center starting 1 day before to 15 days after the mainshock. Template events are selected from the same time period (1 day before mainshocks to 15 days after mainshocks) in the standard SCSN catalog. The number of template events for each aftershock sequence is listed in Table 1. For each template event, we extract template waveforms from all available stations based on the phase data produced by SCSN. For the 2016 sequence we use the refined catalog produced by Ross, Hauksson, and Ben-Zion (2017).

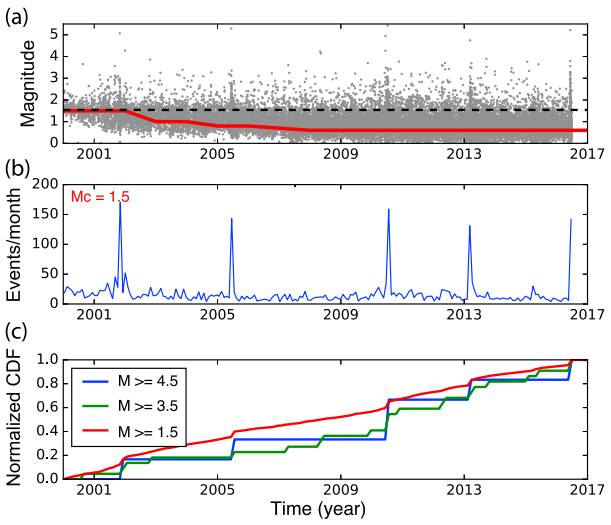

Figure 3. Temporal variation of seismicity in the trifurcation area (events in Figure 1). (a) Earthquake magnitude versus time. Red line shows the estimated magnitude of completeness within a 4-year sliding window. (b) Number of events (M ≥ 1.5) per month within the study area. There are five time periods with a high seismicity rate correspond to M ≥ 4.5 aftershock sequences (Table 1). (c) Normalized cumulative density function (CDF) of seismicity for various minimum magnitude thresholds.

3. Results

3.1. Overview of Seismicity

As mentioned, the trifurcation area of the SJFZ has produced many moderate magnitude earthquakes since 2000. There are 38 M ≥ 4 earthquakes within the trifurcation area in the SCSN catalog (Figure S3) from 1932 to 2016 (85 years), with 10 occurring from 2000 to 2016 (17 years). Moreover, 4 out of 6 $M_L \geq 5$ earthquakes in the trifurcation area from 1932 to 2016 occurred after 2000 (Figures S1 and S3). Figures 1 and 2 provide a map view and projection on vertical cross sections (A-A′ and B-B′) of the 2000–2016 seismicity from the Hauksson et al. (2012) catalog. Most M > 4.5 earthquakes are located near the main faults with depth between 10 to 14 km, while most M < 4.5 events are broadly distributed and occasionally form localized structures with various trends and depths. Most events shallower than 11 km are located on the northeast and southwest sides of the Buck Ridge and Coyote Creek faults, respectively, and are aligned normal to the main faults. In contrast, events deeper than 11 km are located between the Buck Ridge and Coyote Creek faults and delineate the depth variation of the bottom of the seismogenic zone (Figure 2b).

The temporal evolution of seismicity within the region also shows multiple interesting patterns (Figure 3). Due to temporal variations of the seismic

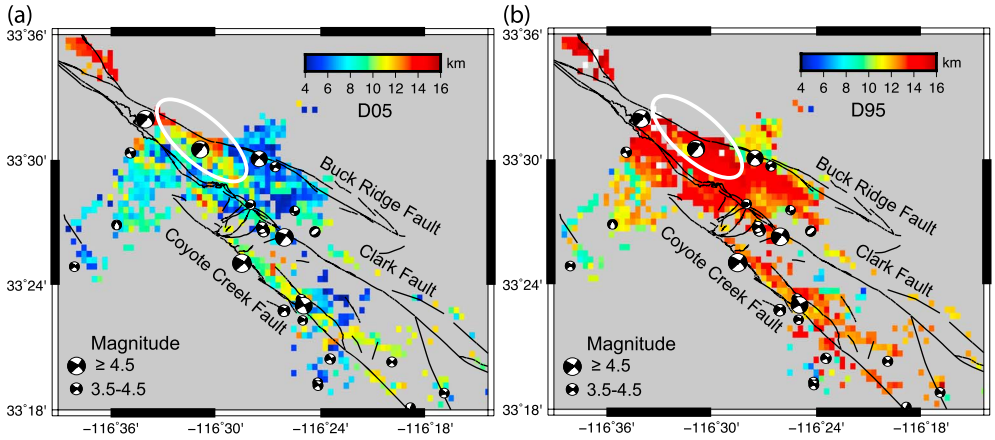

Figure 4. (a) D05 and (b) D95 distribution over a 0.005° × 0.005° (0.465 × 0.556 km) grid. M ≥ 3.5 events are denoted by their focal mechanisms and scaled by magnitude. White ellipses highlight the deep seismogenic zone between the Buck Ridge and Clark faults.

network stations in Southern California, we use a 4-year moving time window to estimate the magnitude of completeness based on the maximum curvature method (Woessner & Wiemer, 2005). For consistency, we select M_C = 1.5 to perform further temporal analysis over the examined time range. It is interesting to note that the five events with M ≥ 4.5 are quasi-periodic in time (Figures 3b and 3c), while the small events with M ≥ 1.5 approximately follow a constant seismicity rate (red line in Figure 3c).

In the following sections, we examine in more detail relations between different aspects of the SJFZ in the trifurcation area and spatiotemporal aspects of seismicity in different magnitude ranges.

3.2. Lateral Variation of Focal Depths

Figure 4 shows the 5th percentile (D05) and 95th percentile (D95) of focal depths of events in the relocated regional catalog on a 0.005° × 0.005° (0.465 × 0.556 km) grid in the trifurcation area. The focal depths exhibit strong lateral variation across the trifurcation area. The D05 distribution is very shallow (~5 km) around the Buck Ridge fault, but parts of the area between the Buck Ridge and Clarks faults have D05 deeper than 11 km (white circle in Figures 4a and 4b). The D95 distribution is a proxy for the bottom of seismogenic zone and may be compared to the geodetically inferred locking depth (~11 km; Fialko, 2006; Wdowinski et al., 2007). We note that regions close to the main faults tend to have D95 values that are less than the locking depth, while regions between the main faults tend to have D95 values that are deeper than the locking depth. Clear examples of this are the strong changes in D95 across the Buck Ridge and Coyote Creek faults. Additionally, most large (M ≥ 4.5) events are along the main faults with strike-slip focal mechanisms. In contrast, some of the mechanisms of the smaller events are normal faulting and they occur between the main faults (Figures 4a and 4b).

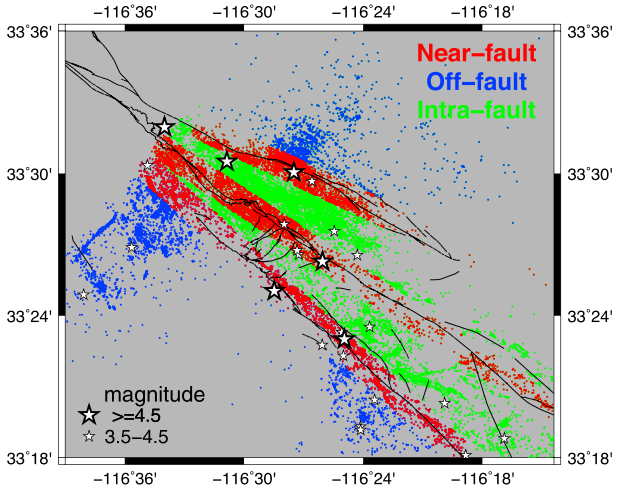

Figure 5. Map view of seismicity colored by the relative distance from the main faults. Red dots denote events within 1-km distance from the main faults (near-fault area). Blue dots are events outside of the fault zone with distance more than 1 km from the main faults (off-fault area). Green dots show events between main faults with distance more than 1 km from the mapped main faults (intra-fault area). M ≥ 3.5 events are denoted by white stars and scaled by size.

3.3. Variations of Focal Mechanisms

Bailey et al. (2010) showed that the SJFZ is associated with high diversity of focal mechanisms. To examine focal mechanisms in relation to the main faults in the trifurcation area, we divide the earthquakes into three groups based on their distance to the main faults: (1) events with distance <1 km to the three primary faults (near-fault area, red dots in Figure 5), (2) events outside of the Buck Ridge and Coyote Creek faults with distance >1 km to the nearest main faults (off-fault area, blue dots in Figure 5), and (3) events between the Buck Ridge

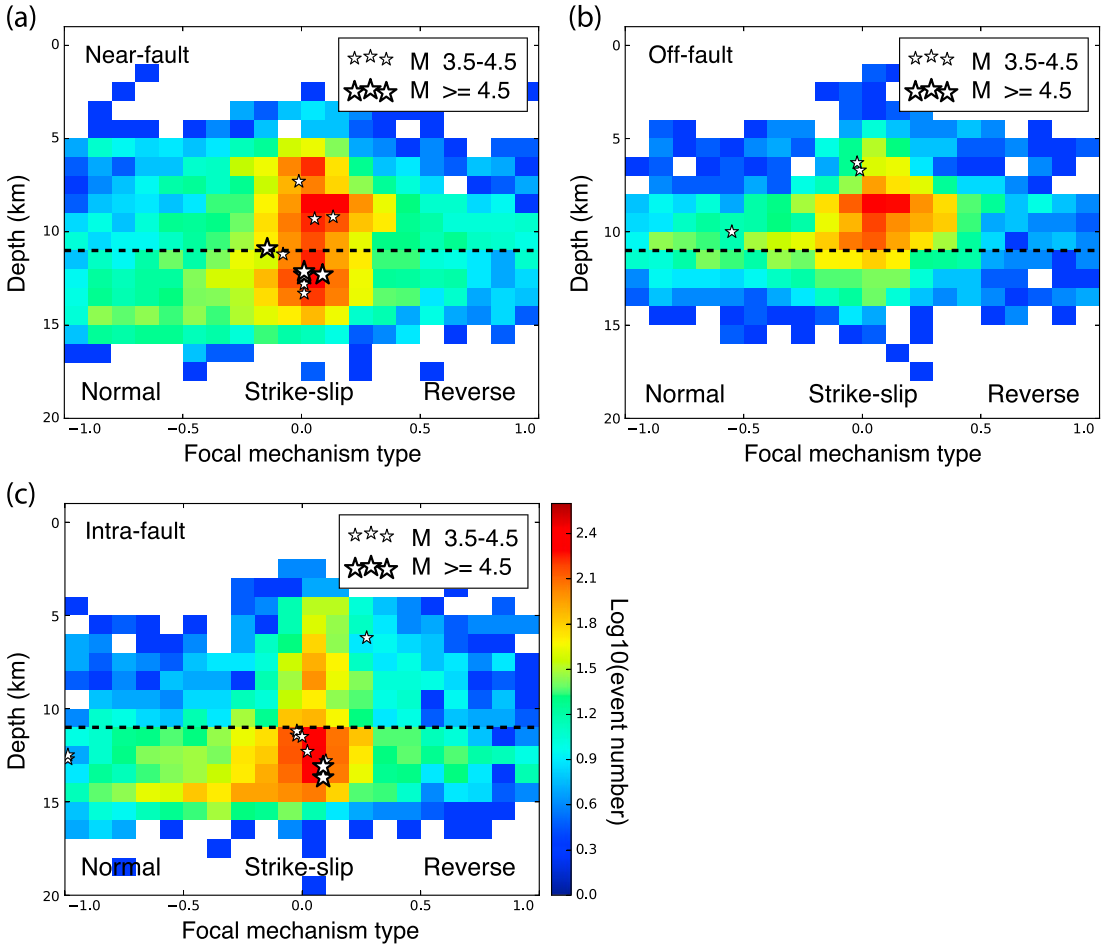

Figure 6. Distribution of focal mechanisms for each depth interval within the near-fault (a), off-fault (b), and intrafault (c) areas. Dashed lines indicate the estimated geodetic locking depth from Fialko (2006).

and Coyote Creek faults with distance >1 km from the main faults (intrafault area, green dots in Figure 5). The events in these categories have different focal depths, faulting types, and magnitudes. Because of the large number and diversity of focal mechanism solutions, it is hard to use scatter plots to compare results between these categories. We therefore first normalize the observed rake angles and express the mechanisms on a continuous scale from −1 to 1, with normal faulting having a value of −1, strike-slip denoted by 0 and thrust faulting denoted by 1 (Shearer et al., 2006).

Figure 6 displays depth-faulting-type 2-D histograms. The focal mechanisms are subdivided into depth and faulting type bins of width 1 km and 0.1 units, respectively, with the estimated geodetic locking depth indicated by a dashed line. The results show clear differences among the three groups. The events in the near-fault region are widely distributed in depth (Figure 6a). Because the seismogenic depth changes abruptly across the main faults, the depth distribution of seismicity on the main faults is hard to define using small magnitude events in the near-fault region. However, as shown by Ross, Hauksson, and Ben-Zion (2017), near-fault $M \geq 3.5$ magnitude events are more likely to occur on the main faults. Most $M \geq 3.5$ near-fault events (white stars in Figure 6a) are around the estimated geodetic locking depth between 11 to 13 km depth (dash lines in Figure 6a), and the focal mechanisms of $M \geq 3.5$ near-fault events are aligned with the direction of mapped main faults (focal mechanisms in Figure 4).

While all $M \geq 4.5$ earthquakes in the near-fault region are deeper than 11 km (Figure 6a), most off-fault events are above 11 km (Figure 6b). Moreover, events in the off-fault region show structures normal to the primary faults (Figure 5). The depth discrepancy between large near-fault events and the near-normal off-fault seismicity suggests that these off-fault events may not be related to the large events along the main faults. The

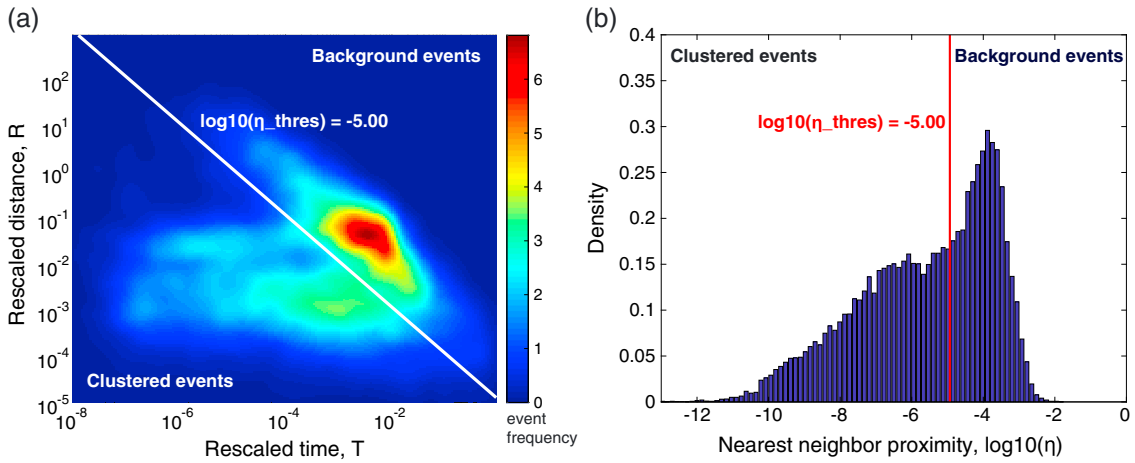

Figure 7. (a) Distribution of nearest-neighbor statistics for all available events in the trifurcation area of the San Jacinto fault zone (2000–2016) with magnitude cutoff M_{min} = 0. The white line shows the nearest-neighbor distance threshold used for clustering (based on the method in Zaliapin & Ben-Zion, 2016). (b) Histogram of nearest-neighbor distance η of all used events. Red line denotes the nearest-neighbor distance threshold used for clustering.

intrafault events are generally concentrated below 11 km depth and are even deeper than in the near-fault region. There are few intrafault events in the top 11 km (Figure 6c). Below 13 km depth, there are many normal faulting events, as well as two M ≥ 4.5 oblique reverse strike-slip events (Figure 6c). Most of these deep events are located at the northwest part of the trifurcation area near the Anza gap (white circle in Figures 4a and 4b). The focal mechanism heterogeneity and deeper focal depths indicate a deformation environment that is distinct from that of the three main faults.

The results in this section are determined using assumed fault zone width of 1 km. To test the sensitivity of the results to other values, we perform corresponding analyses using different fault zone widths (0.5, 1, and 1.5 km). As the assumed fault zone width increases, more events are included in the near-fault group and fewer are included in the intrafault and off-fault groups. However, the observed patterns are generally similar (Figures S4–S6). In particular, the depth-faulting-type distribution of each group is generally insensitive to the employed fault zone width.

3.4. Spatial Patterns of Aftershocks

The previous observations demonstrate that off-fault and intrafault events have significantly different spatial and focal mechanism patterns from near-fault events. We can further analyze volumetric faulting characteristics by exploring the interaction between large strike-slip events and their aftershocks in the surrounding area. To separate aftershocks from background events, we use the cluster detection approach of Zaliapin and Ben-Zion (2013) based on nearest-neighbor distances in a combined space-time-magnitude domain. For each event pair i and j, we calculate,

$$\eta_{ij} = \begin{cases} t_{ij}\left(r_{ij}\right)^{d} 10^{-bm_i}, & t_{ij} > 0; \\ \infty, & t_{ij} \leq 0. \end{cases} \quad (1)$$

where $t_{ij} = t_j - t_i$ is the interevent time, r_{ij} is the interevent distance, d is the fractal dimension of hypocenters, b is the parameter of Gutenberg-Richter distribution, and m_i is the magnitude of event i. The nearest neighbor of event j is the previous event i with the smallest distance based on equation (1). η_{ij} can be represented in terms of space and time components normalized by the magnitude of the earlier event i:

$$T_{ij} = t_{ij}10^{-qbm_i}, R = r_{ij}^{d}10^{-(1-q)bm_i}, 0 < q < 1. \quad (2)$$

In this paper, we compute (1) using b = 1, d_f = 1.6, and q = 0.5. The distribution of nearest-neighbor distances is bimodal (Figures 7 and S7), with the largest mode corresponding to background events and the smaller mode corresponding to clustered events (Zaliapin & Ben-Zion, 2013). We separate the two modes by

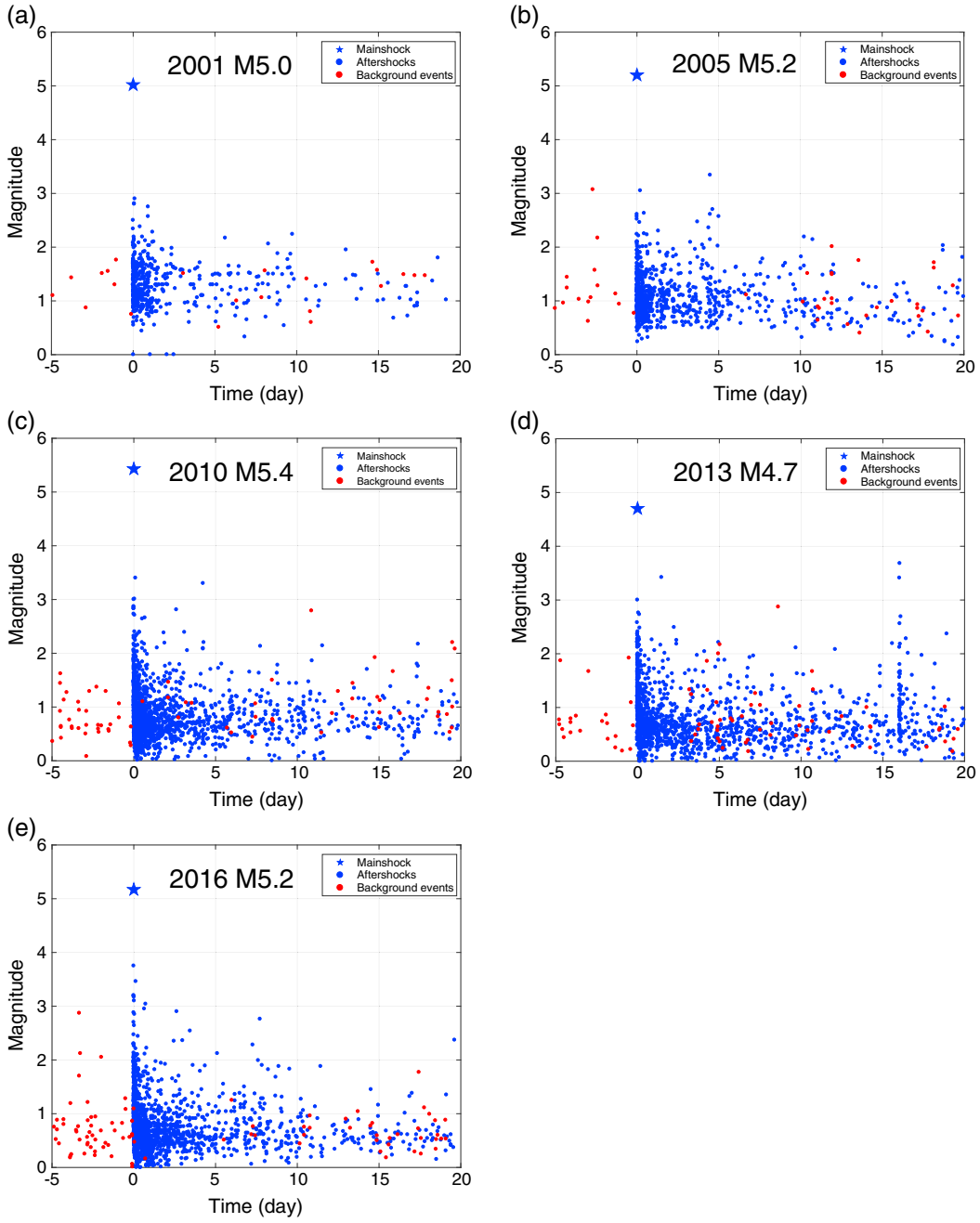

Figure 8. (a–e) Magnitude-time plots of five chosen M > 4.5 aftershock sequences. Most events within 15 days of a mainshock (blue stars) are classified as aftershocks (blue dots) and only a few of them are background events (red dots).

fitting a Gaussian mixture model and choosing the midpoint between the two modes as the threshold for clustering (Zaliapin & Ben-Zion, 2016).

We use catalogs with multiple cutoff magnitudes (0.0, 0.5, 1.0, 1.5) to examine the variation of the distribution of nearest-neighbor distances (Figure S7). The results show that the threshold of nearest-neighbor distances is stable with respect to the magnitude cutoff. As representative analysis we use the threshold $\eta_{\text{thres}} = 10^{-5.00}$ to detect earthquake clusters. Each event is linked to their nearest neighbor (parent) if η_{ij} is smaller than the chosen threshold η_{thres}. The five largest event clusters are found to be associated with the M > 4.5 aftershock sequences (Figure 8). For each mainshock, most events within 1 day before to 15 days after the mainshock are in the same cluster as the mainshock. We therefore use events from the same time window for each

mainshock (1 day before to 15 days after mainshock) and regard them as an earthquake sequence to analyze (Table 1).

For each earthquake sequence, we apply a matched filter method to detect previously unidentified earthquakes in the continuous data following Ross, Hauksson, and Ben-Zion (2017). First, waveforms are downsampled to 50 Hz and band-pass filtered from 2 Hz to 15 Hz. Then, template waveforms are prepared using a 2.5 s time window for the *P* wave and a 4.0 s window for the *S* wave, starting 0.2 s before the analyst's pick. Templates are formed from all channel and phase combinations. Cross correlations between the template waveforms and continuous data are computed in 24-hr segments, using only matching channels. All cross-correlation functions are shifted back in time by the observed travel time of the template and summed up for detection. The detection threshold is either 9 times the median absolute deviation for the respective day or 0.4 if greater. We further require that at least four of the individual phase correlation functions have a peak absolute value of at least 8 times the median absolute deviation to ensure that the stacked correlation function is not dominated by a small number of phases. Detections separated by less than 2 s apart are linked, and the template with the largest stacked cross-correlation coefficient is selected as the reference for single detection. Magnitudes are estimated from the median peak amplitude ratio between detected phase and template phase under the assumption that 1 unit magnitude difference corresponds to a factor of 10 in amplitude ratio.

For each detected event, we first set its initial location to that of the best matching template event. Then we calculate cross correlation coefficients between detected events with their 200 nearest template events (in spatial distance) on all three components using 1.0 s time windows for *P* waves and 1.5 s for *S* waves (e.g., Hauksson et al., 2012). For each station, the largest positive cross-correlation coefficient of each phase is saved. If there are more than 5 differential times with cross-correlation coefficients larger than 0.6 for a given event pair, we use the differential times of this event pair for relocation process. To ensure consistency among the mainshocks and their aftershocks, we use nonrelocated locations from the standard SCSN catalog as the initial locations and the SCSN 1-D velocity model (Table S1) for relocation (Hutton et al., 2010).

The relocation employs the GrowClust algorithm (Trugman & Shearer, 2017a) with a minimum correlation coefficient of 0.6 and a minimum of 6 differential times as input parameters. Newly detected events that are not relocated by GrowClust are removed from further consideration. The total number of events for each sequence before and after detection and relocation is listed in Table 1. The obtained catalogs contain at least 7 times more earthquakes than the SCSN catalog in the same space-time window (Table 1). The location errors of each sequence were estimated by the nonparametric bootstrapped error estimation procedure in GrowClust (Figure S8). In addition to uncertainty introduced from the velocity model and the relocation procedure, variations in the station distribution for each sequence (Figure S2) can also lead to inconsistencies between the resulting seismicity patterns. To check the influence of station distribution on earthquake relocation, we use a fixed set of stations (Figure S2a) to conduct the relocation of all sequences. Figure S9 compares the relocation results derived with all available stations to those obtained using the stations in Figure S2a. The results demonstrate that the overall characteristics of the obtained sequences discussed in the paper are not sensitive to the station distribution. This is probably due to the fact that most nearby stations have been available from 2001 to 2016.

The aftershock sequences in the updated catalogs exhibit a variety of noteworthy patterns (Figure 9). One striking observation is that for each $M \geq 5$ aftershock sequence, more than 98% of the events are at least 1 km epicentral distance from the mainshock (solid-line circles in Figures 9a to 9e). There also is no obvious fault plane structure among the seismicity for any mainshock. If we take the horizontal location errors of aftershocks ε_{AFS} (Figure S8) and mainshocks ε_{MS} (Table 2) into consideration, the errors ε_{dist} between each mainshock's horizontal location $\boldsymbol{x}_{MS}$ and its aftershocks' horizontal locations $\boldsymbol{x}_{AFS}$ can be roughly estimated using

$$\varepsilon_{dist} = \varepsilon\left(\overrightarrow{x}_{MS} - \overrightarrow{x}_{AFS}\right) \leq \varepsilon(x_{MS} - x_{AFS}) = \sqrt[2]{\varepsilon_{AFS}^2 + \varepsilon_{MS}^2}. \quad (3)$$

The calculated epicentral distance errors of aftershock sequences are shown in Table 2. At least 70% of the events are more than 1-km epicentral distance from their respective mainshock (dashed-line circles in Figures 9a–9c and 7e). The 2013 M4.7 event has about 60% of the aftershocks more than 1-km distance away

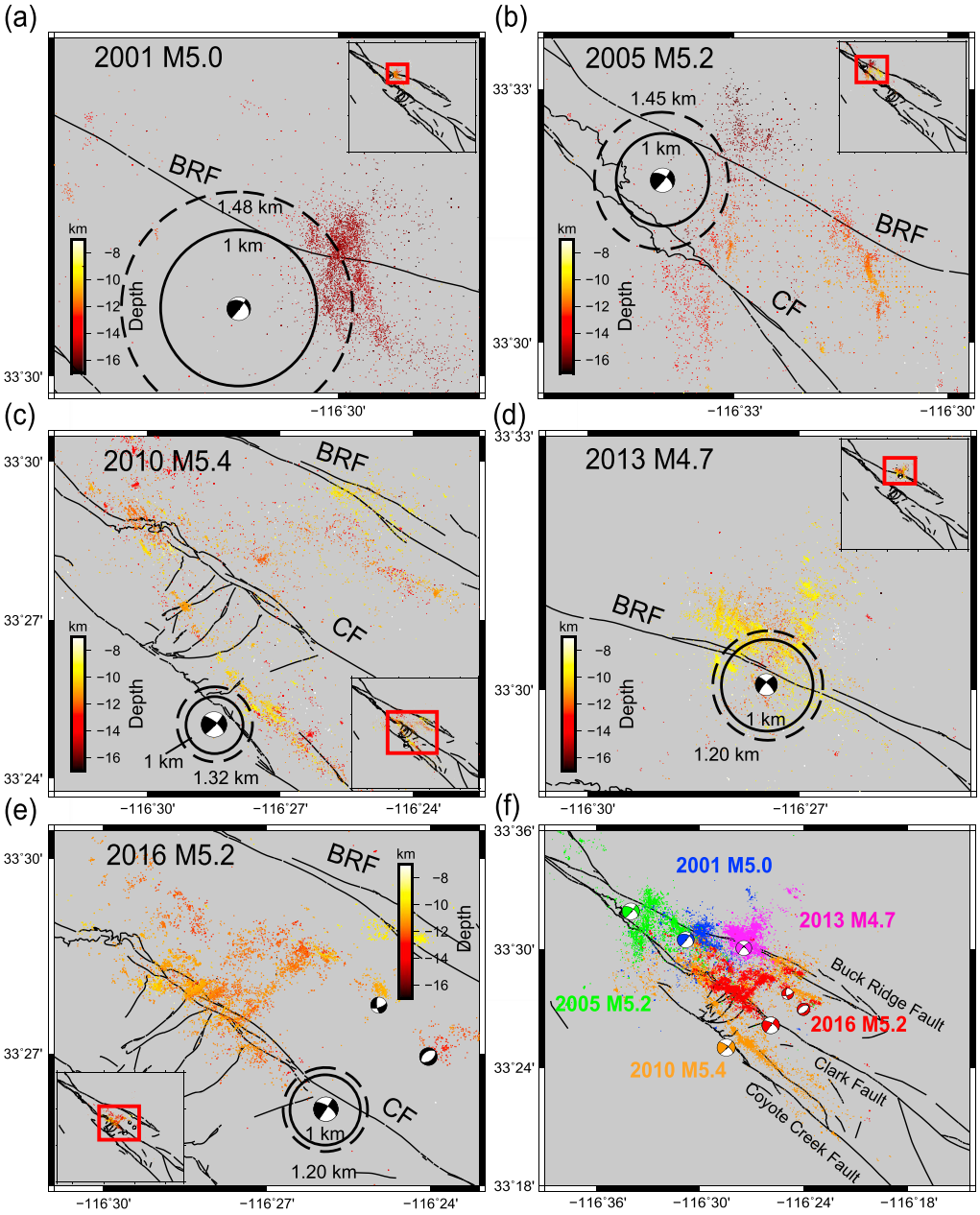

Figure 9. (a–f) Map views of seismicity for the five main sequences. Large magnitude events (M ≥ 3.5) are shown as focal mechanisms. Note the lack of aftershocks within 1 km of each mainshock (solid circles; dashed circles have radiuses of 1 km plus the estimated mainshock-aftershock distance errors, respectively).

(Table 2). Ross, Kanamori, and Hauksson (2017) noted this feature for the 2016 sequence and showed that this gap was coincident with the coseismic slip distribution of the mainshock. They further argued that the lack of aftershocks within the slip zone and large stress drop (~80 MPa) suggests that the residual stress on the fault is low. Besides the 2016 sequence, Trugman and Shearer (2017b) observed that the stress drops of these mainshocks are quite large, which is consistent with the generally large mainshock-aftershock distances of all examined aftershock sequences (Figure 9). Similar observations for global megathrust earthquakes were analyzed by Wetzler et al. (2018).

The newly detected aftershocks also delineate numerous structures with various orientations. Interestingly, none of these aftershock sequences share a similar spatial pattern. The aftershocks of the 2001 M5.0 event

Table 2
Horizontal Location Errors of Chosen Aftershock Sequences, Estimated Mainshock-Aftershock Epicentral Distance Errors, and the Percentage of Aftershocks With Epicentral Distance >1 km

Event	Mainshock horizontal errors (km)	90th percentile aftershocks horizontal errors (km)	Epicentral distance error (km)	Percentage of aftershocks with epicentral distance >1 km (without consideration of location errors)	Percentage of aftershocks with epicentral distance <1 km (with consideration of location errors)
2001 M5.2	0.26	0.41	0.48	97.3%	72.9%
2005 M5.0	0.16	0.42	0.45	98.7%	95.6%
2010 M5.4	0.17	0.27	0.32	99.9%	99.5%
2013 M4.7	0.14	0.14	0.20	77.8%	61.5%
2016 M5.2	0.13	0.15	0.20	99.9%	99.8%

are clustered together without any clear lineations (Figure 9a). The 2005 and 2010 sequences are distributed sparsely in space and show some linear structures at an oblique angle to the main faults (Figures 9b and 9c). In contrast, the 2013 and 2016 sequences are highly clustered with abundant small scale lineations that are almost orthogonal to the main faults (Figures 9d and 9e). Despite the broad distribution of aftershocks and diverse seismicity patterns, only a few aftershocks are located near the main faults and a limited number of the lineations are oriented parallel to the main faults (Figures 9a–9e). Additionally, while each aftershock distribution covers a broad area, they only have limited overlap in space (Figure 9f). The lack of overlap and the fact that the sequences occur only a few years apart suggest that each aftershock zone has a different stress distribution. This is most prominent when comparing the 2010 and 2016 sequences, where the 2010 aftershock distribution "bends" around the eventual site of the 2016 aftershock distribution. These diverse patterns provide clear evidence for the complex volumetric interactions of earthquakes in the region.

Although all mainshock hypocenters have depths between 11 km to 14 km, the depth ranges of their aftershock sequences are much broader. Most aftershocks of the 2001 M5.0 and 2005 M5.2 aftershock sequences in the intrafault area at the northwest between the Buck Ridge and Coyote Creek faults are between 13 and 17 km (Figures 9a and 9b). The 2013 M4.7 event along the Buck Ridge fault triggered many off-fault aftershocks on the northeast side with depth shallower than 11 km (Figure 9d). The 2010 M5.4 and 2016 M5.2 events produced a large number of intermediate-depth (10–15 km) aftershocks (Figures 9e and 9f). These results are consistent with the observation from the entire relocated catalog that off-fault aftershocks are shallower than 11 km, while the intrafault region has aftershocks deeper than 11 km. Horizontally, the aftershock patterns exhibit a strong correlation with the focal mechanisms of their mainshocks. The 2001 M5.0 and 2005 M5.2 events are oblique reverse-strike-slip events followed by many aftershocks deeper than 13 km on the east side of their mainshocks (Figures 9a and 9b). The 2010 M5.4, 2013 M4.7, and 2016 M5.2 events share similar focal mechanisms and produce aftershocks on the northwest of mainshocks, despite their different locations, magnitudes, and depths (Figures 9c–9e).

4. Discussion and Conclusions

We perform several types of analyses to clarify basic aspects of earthquake and fault mechanics in the trifurcation area of the SJFZ using relocated seismicity, focal mechanisms, and detection of additional aftershocks for five $M > 4.5$ earthquakes. Both the historical seismicity and focused analyses of moderate aftershock sequences illustrate the complexity and essential volumetric characteristics of tectonic deformation in the region. Spatiotemporal variations of seismicity, magnitudes, and source mechanisms highlight the importance of distinguishing between failure processes associated with the main faults and those occurring in the surrounding crustal volumes.

There are various general reasons for complex volumetric behavior of earthquakes of the type documented in this paper (Figure 9). On an elementary level, tendencies of dynamic ruptures to branch from a fault during propagation (e.g., Sharon et al., 1995; Yoffe, 1951) and to generate high-angle off-fault fractures near barriers (e.g., S. Xu & Ben-Zion, 2013) can produce off-fault complexity even in a homogenous solid under single-mode loading. More importantly, preexisting structural heterogeneities and mixed-mode loadings, which are common in the crust, can prevent localization of deformation and produce seismic responses over a

network of faults and fracture zones (e.g., Finzi et al., 2009; Lyakhovsky & Ben-Zion, 2008). Aftershocks generally occupy volumes around mainshock ruptures and produce distributed rock damage that can delocalize the earthquake deformation zone. Aftershocks in the lower crust due to transient deepening of the brittle-ductile transition after large mainshocks (e.g., Ben-Zion & Lyakhovsky, 2006; McNamara et al., 2017; Rolandone et al., 2004), and related changes of rock type and dynamics of the lower crust (e.g., Jamtveit et al., 2018), can also broaden the seismic deformation zone. In the trifurcation area of the SJFZ, likely major contributing factors to the observed volumetric failure patterns are the complex geometry of the fault system with three main faults (Buck Ridge, Clark, and Coyote Creek) and many subsidiary structures including some orthogonal to the main faults (Figure 1), shear loading of the plate-boundary combined with opening in the Gulf of California (e.g., Axen & Fletcher, 1998) and possible additional transient loadings from ductile shear zones off the main faults.

A number of recent studies showed that the three main faults in the trifurcation area have strong velocity contrasts and asymmetric damage zones concentrated on the northeast sides of the faults (Allam et al., 2014; Qin et al., 2018; Qiu et al., 2017). The large available surface areas along the main faults allow for the occurrence of relatively large events. Almost all near-fault M $\geq$3.5 earthquakes are right-lateral strike-slip events with strike direction consistent with the plate-boundary shear deformation (focal mechanisms in Figure 4). Most large ruptures are concentrated between 11 km to 13 km depth near the bottom of the near-fault seismicity and the geodetic locking depth (Figure 6a). Some of these near-fault mainshocks (Figures 9–9e) triggered a large number of aftershocks on the northeast sides of their rupture zones. Some historical moderate events in trifurcation area like the 1937 Buck Ridge earthquake and 1980 Whitewash earthquake also have right-lateral focal mechanisms with abundant aftershocks to the northeast of the main faults (Sanders et al., 1986; Sanders & Kanamori, 1984).

The intrafault and off-fault areas have complex smaller-size faults and fractures with distributed seismicity at different depth sections and various focal mechanisms (Figure 6). Bailey et al. (2010) analyzed focal mechanism heterogeneity in the SJFZ and suggested that it is controlled primarily by fault zone structure rather than time or magnitude. The distributed cracking in the intrafault and off-fault regions produce collectively damage zones manifested by reduced seismic velocities and anomalous Vp/Vs ratios (Allam et al., 2014; Zigone et al., 2015). The intrafault mainshocks have some different characteristics from the near-fault mainshocks. The 2001 M5.0 and 2005 M5.2 events have hypocenters below 13 km and oblique reverse-strike-slip mechanisms. The spatial distributions of these aftershock sequences do not exhibit along-strike asymmetry with respect to the mainshock as seen for the moderate five mainshocks and other events on main fault sections (Zaliapin & Ben-Zion, 2011). These two aftershock sequences are located at the northwest of the trifurcation area and are deeper than other aftershock sequences on the main faults. The different depths may be related to the fact that the seismogenic zone is becoming overall shallower to the southwest likely because of regional variations of heat flow (Doser & Kanamori, 1986; Sibson, 1984). In addition, these two events may occur along large thrust faults around the restraining bend formed by left stepping of the Buck Ridge fault that may cause a deepening of the seismogenic zone (Sibson, 1984). The abundant normal faulting events in the intrafault area (Figure 6c) and numerous near-orthogonal structures delineated by the aftershock sequences (Figures 9a–9e) demonstrate the broad damage zone between the main fault segments. Events with purely extensional normal faulting mechanisms indicate small-scale pull-apart structures between parallel fault segments. For events deeper than 13 km, there are increasing numbers of normal mechanisms and decreasing numbers of strike-slip events.

The five recent M $>$ 4.5 mainshocks have aftershock sequences with only a little spatial overlap, and four M $\geq$ 5 mainshocks have more than 70% of the aftershocks at least 1-km epicentral distance from their mainshock hypocenters (Figure 9). The lack of aftershocks near the mainshock hypocenters is consistent with the large stress drops in the range 80–150 MPa found for the mainshocks (Ross & Ben-Zion, 2016; Trugman & Shearer, 2017b; Ross, Kanamori, & Hauksson, 2017), while the occurrence of distinct sequences with little spatial overlap point to significant regional heterogeneities. As shown by Ross, Hauksson, and Ben-Zion (2017), most of the background seismicity in the area occurs within off-fault damage zones, implying that the main faults are locked. These broad damage zones extend down to 15 km and coincide with Vp/Vs anomalies (Allam et al., 2014). The discrepancy between the locking depth of the main faults and maximum depth of seismicity is largely a consequence of projecting all the events to the main fault surfaces. As shown in Figure 4b, the depth of seismicity in the near-fault region is consistent with the geodetically inferred

locking depth. This eliminates the need for a deep creeping zone to reconcile the difference between locking depth and maximum depth of seismicity. However, a deep creeping zone may still exist as suggested by the long duration and along-strike spatial extent of aftershock zones of some of the $M > 4.5$ events (Wdowinski, 2009; Meng & Peng, 2016; Ross, Hauksson, & Ben-Zion, 2017) and possible slow slip events triggered by the 2010 M_w 7.2 El Mayor-Cucapah earthquake and recent $M > 5$ mainshocks in the area (Inbal et al., 2017).

The observations examined in this study reflect processes that occur in different crustal volumes. The majority of events within the damage zone differ from the larger events on the main faults in many aspects including focal mechanisms, stress drops, and geometric complexity. The diverse seismicity structures, large aftershock zones with little spatial overlap, long-duration sequences, and significant distance between mainshocks and aftershocks point to complex interactions between the main faults and the surrounding damage zones. The low level of low magnitude seismicity on the primary faults and large seismicity gaps around the $M > 4.5$ mainshocks suggests that the main fault structures in the area are locked in agreement with geodesy. The increasing rate of moderate strike-slip events between 10 to 13 km depth near the main faults, productive aftershock sequences and large lapse time since the last major San Jacinto fault zone earthquake, suggests that the region may be approaching the next major earthquake. At the same time, the barely overlapping aftershock sequences of the analyzed $M > 4.5$ events point to the significant heterogeneity and complex dynamics of earthquakes in the most seismically active fault zone in southern California. Describing deformation in the SJFZ (and other large fault zones) as occurring on a single fault surface can obscure essential aspects of the dynamics. Improving the understanding of evolutionary processes leading to major earthquakes requires volumetric frameworks that account for different processes occurring on main faults and their surrounding regions.

Acknowledgments
The study was supported by the National Science Foundation (grants EAR-1551411 and EAR-1722561). The paper benefitted from comments by Shimon Wdowinski, an anonymous referee, and the Associate Editor. The waveform data and initial seismicity catalogs used are publicly available via the Southern California Earthquake Data Center (2013) (scedc.caltech.edu). The seismicity catalogs produced in this study are available in the supporting information, with the exception of the 2016 sequence which is available in the open-access supporting information of Ross, Hauksson, and Ben-Zion (2017).

References

Allam, A. A., Ben-Zion, Y., Kurzon, I., & Vernon, F. (2014). Seismic velocity structure in the Hot Springs and Trifurcation areas of the San Jacinto fault zone, California, from double-difference tomography. *Geophysical Journal International*, *198*(2), 978–999. https://doi.org/10.1093/gji/ggu176

Asano, K., & Iwata, T. (2016). Source rupture processes of the foreshock and mainshock in the 2016 Kumamoto earthquake sequence estimated from the kinematic waveform inversion of strong motion data. *Earth, Planets and Space*, *68*(1), 147. https://doi.org/10.1186/s40623-016-0519-9

Axen, G. J., & Fletcher, J. M. (1998). Late Miocene-Pleistocene extensional faulting, northern Gulf of California, Mexico and Salton Trough, California. *International Geology Review*, *40*(3), 217–244. https://doi.org/10.1080/00206819809465207

Bailey, I. W., Ben-Zion, Y., Becker, T. W., & Holschneider, M. (2010). Quantifying focal mechanism heterogeneity for fault zones in central and southern California. *Geophysical Journal International*, *183*(1), 433–450. https://doi.org/10.1111/j.1365-246X.2010.04745.x

Ben-Zion, Y. (2008). Collective behavior of earthquakes and faults: Continuum-discrete transitions, progressive evolutionary changes, and different dynamic regimes. *Reviews of Geophysics*, *46*, RG4006. https://doi.org/10.1029/2008RG000260

Ben-Zion, Y., & Ampuero, J. P. (2009). Seismic radiation from regions sustaining material damage. *Geophysical Journal International*, *178*(3), 1351–1356. https://doi.org/10.1111/j.1365-246X.2009.04285.x

Ben-Zion, Y., & Lyakhovsky, V. (2006). Analysis of aftershocks in a lithospheric model with seismogenic zone governed by damage rheology. *Geophysical Journal International*, *165*(1), 197–210. https://doi.org/10.1111/j.1365-246X.2006.02878.x

Ben-Zion, Y., & Sammis, C. G. (2003). Characterization of fault zones. In *Seismic motion, lithospheric structures, earthquake and volcanic sources: The Keiiti Aki Volume* (pp. 677–715). Basel: Birkhäuser. https://doi.org/10.1007/978-3-0348-8010-7_11

Clark, K. J., Nissen, E. K., Howarth, J. D., Hamling, I. J., Mountjoy, J. J., Ries, W. F., et al. (2017). Highly variable coastal deformation in the 2016 Mw7. 8 Kaikōura earthquake reflects rupture complexity along a transpressional plate boundary. *Earth and Planetary Science Letters*, *474*, 334–344. https://doi.org/10.1016/j.epsl.2017.06.048

Doser, D. I., & Kanamori, H. (1986). Depth of seismicity in the Imperial Valley region (1977–1983) and its relationship to heat flow, crustal structure and the October 15, 1979, earthquake. *Journal of Geophysical Research*, *91*(B1), 675–688. https://doi.org/10.1029/JB091iB01p00675

Fay, N. P., & Humphreys, E. D. (2005). Fault slip rates, effects of elastic heterogeneity on geodetic data, and the strength of the lower crust in the Salton Trough region, southern California. *Journal of Geophysical Research*, *110*, B09401. https://doi.org/10.1029/2004JB003548

Fialko, Y. (2006). Interseismic strain accumulation and the earthquake potential on the southern San Andreas fault system. *Nature*, *441*(7096), 968–971. https://doi.org/10.1038/nature04797

Finzi, Y., Hearn, E. H., Ben-Zion, Y., & Lyakhovsky, V. (2009). Structural properties and deformation patterns of evolving strike-slip faults: Numerical simulations incorporating damage rheology. *Pure and Applied Geophysics*, *166*(10–11), 1537–1573. https://doi.org/10.1007/s00024-009-0522-1

Fletcher, J., Haar, L., Hanks, T., Baker, L., Vernon, F., Berger, J., & Brune, J. (1987). The digital array at Anza, California: Processing and initial interpretation of source parameters. *Journal of Geophysical Research*, *92*, 369–382. https://doi.org/10.1029/JB092iB01p00369

Hauksson, E., Jones, L. M., Hutton, K., & Eberhart-Phillips, D. (1993). The 1992 landers earthquake sequence: Seismological observations. *Journal of Geophysical Research*, *98*, 19,835–19,858. https://doi.org/10.1029/93JB02384

Hauksson, E., Yang, W., & Shearer, P. M. (2012). Waveform relocated earthquake catalog for southern California (1981 to June 2011). *Bulletin of the Seismological Society of America*, *102*(5), 2239–2244. https://doi.org/10.1785/0120120010

Hillers, G., Ben-Zion, Y., & Mai, P. M. (2006). Seismicity on a fault controlled by rate- and state-dependent friction with spatial variations of the critical slip distance. *Journal of Geophysical Research*, *111*, B01403. https://doi.org/10.1029/2005JB003859

Hutton, K., Woessner, J., & Hauksson, E. (2010). Earthquake monitoring in southern California for seventy-seven years (1932–2008). *Bulletin of the Seismological Society of America*, *100*(2), 423–446. https://doi.org/10.1785/0120090130

Inbal, A., Ampuero, J.-P., & Avouac, J.-P. (2017). Locally and remotely triggered aseismic slip on the central San Jacinto Fault near Anza, CA, from joint inversion of seismicity and strainmeter data. *Journal of Geophysical Research: Solid Earth*, *122*, 3033–3061. https://doi.org/10.1002/2016JB013499

Jamtveit, B., Ben-Zion, Y., Renard, F., & Austrheim, H. (2018). Earthquake-induced transformation of the lower crust. *Nature*, *556*(7702), 487–491. https://doi.org/10.1038/s41586-018-0045-y

Julian, B. R., Miller, A. D., & Foulger, G. R. (1998). Non-double-couple earthquakes 1. Theory. *Reviews of Geophysics*, *36*, 525–549. https://doi.org/10.1029/98RG00716

Lindsey, E. O., & Fialko, Y. (2013). Geodetic slip rates in the southern San Andreas fault system: Effects of elastic heterogeneity and fault geometry. *Journal of Geophysical Research: Solid Earth*, *118*, 689–697. https://doi.org/10.1029/2012JB009358

Lyakhovsky, V., & Ben-Zion, Y. (2008). Scaling relations of earthquakes and aseismic deformation in a damage rheology model. *Geophysical Journal International*, *172*(2), 651–662. https://doi.org/10.1111/j.1365-246X.2007.03652.x

McNamara, D. E., Yeck, W. L., Barnhart, W. D., Schulte-Pelkum, V., Bergman, E., Adhikari, L. B., et al. (2017). Source modeling of the 2015 M_W 7.8 Nepal (Gorkha) earthquake sequence: Implications for geodynamics and earthquake hazards. *Tectonophysics*, *714-15*, 31–30.

Meng, X., & Peng, Z. (2016). Increasing lengths of aftershock zones with depths of moderate-size earthquakes on the San Jacinto Fault suggests triggering of deep creep in the middle crust. *Geophysical Journal International*, *204*(1), 250–261.

Onderdonk, N. W., Rockwell, T. K., McGill, S. F., & Marliyani, G. I. (2013). Evidence for seven surface ruptures in the past 1600 years on the Claremont fault at Mystic Lake, northern San Jacinto fault zone, California. *Bulletin of the Seismological Society of America*, *103*(1), 519–541. https://doi.org/10.1785/0120120060

Petersen, M. D., & Wesnousky, S. G. (1994). Fault slip rates and earthquake histories for active faults in southern California. *Bulletin of the Seismological Society of America*, *84*(5), 1608–1649.

Qin, L., Ben-Zion, Y., Qiu, H., Share, P. E., Ross, Z. E., & Vernon, F. L. (2018). Internal structure of the San Jacinto fault zone in the trifurcation area southeast of Anza, California, from data of dense seismic arrays. *Geophysical Journal International*, *213*(1), 98–114. https://doi.org/10.1093/gji/ggx540

Qiu, H., Ben-Zion, Y., Ross, Z. E., Share, P. E., & Vernon, F. L. (2017). Internal structure of the San Jacinto fault zone at Jackass Flat from data recorded by a dense linear array. *Geophysical Journal International*, *209*(3), 1369–1388. https://doi.org/10.1093/gji/ggx096

Rockwell, T. K., Dawson, T. E., Ben-Horin, J. Y., & Seitz, G. (2015). A 21-event, 4,000-year history of surface ruptures in the Anza seismic gap, San Jacinto Fault, and implications for long-term earthquake production on a major plate boundary fault. *Pure and Applied Geophysics*, *172*(5), 1143–1165. https://doi.org/10.1007/s00024-014-0955-z

Rolandone, F., Bürgmann, R., & Nadeau, R. M. (2004). The evolution of the seismic-aseismic transition during the earthquake cycle: Constraints from the time-dependent depth distribution of aftershocks. *Geophysical Research Letters*, *31*, L23610. https://doi.org/10.1029/2004GL021379

Ross, Z. E., & Ben-Zion, Y. (2016). Toward reliable automated estimates of earthquake source properties from body wave spectra. *Journal of Geophysical Research: Solid Earth*, *121*, 4390–4407. https://doi.org/10.1002/2016JB013003

Ross, Z. E., Ben-Zion, Y., & Zhu, L. (2015). Isotropic source terms of San Jacinto fault zone earthquakes based on waveform inversions with a generalized CAP method. *Geophysical Journal International*, *200*(2), 1269–1280. https://doi.org/10.1093/gji/ggu460

Ross, Z. E., Hauksson, E., & Ben-Zion, Y. (2017). Abundant off-fault seismicity and orthogonal structures in the San Jacinto fault zone. *Science Advances*, *3*(3), e1601946. https://doi.org/10.1126/sciadv.1601946

Ross, Z. E., Kanamori, H., & Hauksson, E. (2017). Anomalously large complete stress drop during the 2016 M_w 5.2 Borrego Springs earthquake inferred by waveform modeling and near-source aftershock deficit. *Geophysical Research Letters*, *44*(12), 5994–6001. https://doi.org/10.1002/2017GL073338

Sanders, C., Magistrale, H., & Kanamori, H. (1986). Rupture patterns and preshocks of large earthquakes in the southern San Jacinto fault zone. *Bulletin of the Seismological Society of America*, *76*(5), 1187–1206.

Sanders, C. O., & Kanamori, H. (1984). A seismotectonic analysis of the Anza seismic gap, San Jacinto fault zone, southern California. *Journal of Geophysical Research*, *89*, 5873–5890. https://doi.org/10.1029/JB089iB07p05873

Sharon, E., Gross, S. P., & Fineberg, J. (1995). Local crack branching as a mechanism for instability in dynamic fracture. *Physical Review Letters*, *74*(25), 5096–5099. https://doi.org/10.1103/PhysRevLett.74.5096

Shearer, P. M., Prieto, G. A., & Hauksson, E. (2006). Comprehensive analysis of earthquake source spectra in southern California. *Journal of Geophysical Research*, *111*, B06303. https://doi.org/10.1029/2005JB003979

Shirahama, Y., Yoshimi, M., Awata, Y., Maruyama, T., Azuma, T., Miyashita, Y., et al. (2016). Characteristics of the surface ruptures associated with the 2016 Kumamoto earthquake sequence, central Kyushu, Japan. *Earth, Planets and Space*, *68*(1), 191. https://doi.org/10.1186/s40623-016-0559-1

Sibson, R. H. (1984). Roughness at the base of the seismogenic zone: Contributing factors. *Journal of Geophysical Research*, *89*, 5791–5799. https://doi.org/10.1029/JB089iB07p05791

Southern California Earthquake Data Center (2013). Southern California Earthquake Center. California Institute of Technology. Dataset. https://doi.org/10.7909/C3WD3xH1

Thomas, M. Y., Avouac, J. P., & Lapusta, N. (2017). Rate-and-state friction properties of the Longitudinal Valley Fault from kinematic and dynamic modeling of seismic and aseismic slip. *Journal of Geophysical Research: Solid Earth*, *122*, 3115–3137. https://doi.org/10.1002/2016JB013615

Trugman, D. T., & Shearer, P. M. (2017a). GrowClust: A hierarchical clustering algorithm for relative earthquake relocation, with application to the Spanish Springs and Sheldon, Nevada, earthquake sequences. *Seismological Research Letters*, *88*(2A), 379–391. https://doi.org/10.1785/0220160188

Trugman, D. T., & Shearer, P. M. (2017b). Application of an improved spectral decomposition method to examine earthquake source scaling in Southern California. *Journal of Geophysical Research: Solid Earth*, *122*, 2890–2910. https://doi.org/10.1002/2017JB013971

Tse, S. T., & Rice, J. R. (1986). Crustal earthquake instability in relation to the depth variation of frictional slip properties. *Journal of Geophysical Research*, *91*, 9452–9472. https://doi.org/10.1029/JB091iB09p09452

Wdowinski, S. (2009). Deep creep as a cause for the excess seismicity along the San Jacinto fault. *Nature Geoscience*, *2*(12), 882–885. https://doi.org/10.1038/ngeo684

Wdowinski, S., Smith-Konter, B., Bock, Y., & Sandwell, D. (2007). Diffuse interseismic deformation across the Pacific–North America plate boundary. *Geology*, *35*(4), 311–314. https://doi.org/10.1130/G22938A.1

Wei, M., Sandwell, D., Fialko, Y., & Bilham, R. (2011). Slip on faults in the Imperial Valley triggered by the 4 April 2010 Mw 7.2 El Mayor-Cucapah earthquake revealed by InSAR. *Geophysical Research Letters*, *38*, L01308. https://doi.org/10.1029/2010GL045235

Wetzler, N., Lay, T., Brodsky, E. E., & Kanamori, H. (2018). Systematic deficiency of aftershocks in areas of high coseismic slip for large subduction zone earthquakes. *Science Advances*, *4*(2), eaao3225. https://doi.org/10.1126/sciadv.aao3225

Woessner, J., & Wiemer, S. (2005). Assessing the quality of earthquake catalogues: Estimating the magnitude of completeness and its uncertainty. *Bulletin of the Seismological Society of America*, *95*(2), 684–698. https://doi.org/10.1785/0120040007

Xu, S., & Ben-Zion, Y. (2013). Numerical and theoretical analyses of in-plane dynamic rupture on a frictional interface and off-fault yielding patterns at different scales. *Geophysical Journal International*, *193*(1), 304–320. https://doi.org/10.1093/gji/ggs105

Xu, W., Feng, G., Meng, L., Zhang, A., Ampuero, J. P., Bürgmann, R., & Fang, L. (2018). Transpressional rupture cascade of the 2016 Mw 7.8 Kaikoura earthquake, New Zealand. *Journal of Geophysical Research: Solid Earth*, *123*, 2396–2409. https://doi.org/10.1002/2017JB015168

Yang, W., Hauksson, E., & Shearer, P. M. (2012). Computing a large refined catalog of focal mechanisms for southern California (1981–2010): Temporal stability of the style of faulting. *Bulletin of the Seismological Society of America*, *102*(3), 1179–1194. https://doi.org/10.1785/0120110311

Yoffe, E. H. (1951). The moving Griffith crack. *Philosophical Magazine*, *42*(330), 739–750. https://doi.org/10.1080/14786445108561302

Yue, H., Lay, T., & Koper, K. D. (2012). En échelon and orthogonal fault ruptures of the 11 April 2012 great intraplate earthquakes. *Nature*, *490*(7419), 245–249. https://doi.org/10.1038/nature11492

Zaliapin, I., & Ben-Zion, Y. (2011). Asymmetric distribution of aftershocks on large faults in California. *Geophysical Journal International*, *185*(3), 1288–1304. https://doi.org/10.1111/j.1365-246X.2011.04995.x

Zaliapin, I., & Ben-Zion, Y. (2013). Earthquake clusters in southern California I: Identification and stability. *Journal of Geophysical Research: Solid Earth*, *118*, 2847–2864. https://doi.org/10.1002/jgrb.50179

Zaliapin, I., & Ben-Zion, Y. (2016). A global classification and characterization of earthquake clusters. *Geophysical Journal International*, *207*(1), 608–634. https://doi.org/10.1093/gji/ggw300

Zigone, D., Ben-Zion, Y., Campillo, M., & Roux, P. (2015). Seismic tomography of the Southern California plate boundary region from noise-based Rayleigh and love waves. *Pure and Applied Geophysics*, *172*(5), 1007–1032. https://doi.org/10.1007/s00024-014-0872-1

Zöller, G., & Ben-Zion, Y. (2014). Large earthquake hazard of the San Jacinto fault zone, CA, from long record of simulated seismicity assimilating the available instrumental and paleoseismic data. *Pure and Applied Geophysics*, *171*(11), 2955–2965. https://doi.org/10.1007/s00024-014-0783-1